

# Effective Solid State LiDAR Odometry Using Continuous-time Filter Registration

Xin Zheng, Jianke Zhu, *Senior Member, IEEE*

**Abstract**—Solid-state LiDARs are more compact and cheaper than the conventional mechanical multi-line spinning LiDARs, which have become increasingly popular in autonomous driving recently. However, there are several challenges for these new LiDAR sensors, including severe motion distortions, small field of view and sparse point cloud, which hinder them from being widely used in LiDAR odometry. To tackle these problems, we present an effective continuous-time LiDAR odometry (ECTLO) method for the Risley prism-based LiDARs with non-repetitive scanning patterns. To account for the noisy data, a filter-based point-to-plane Gaussian Mixture Model is used for robust registration. Moreover, a LiDAR-only continuous-time motion model is employed to relieve the inevitable distortions. To facilitate the implicit data association in parallel, we maintain all map points within a single range image. Extensive experiments have been conducted on various testbeds using the solid-state LiDARs with different scanning patterns, whose promising results demonstrate the efficacy of our proposed approach.

**Index Terms**—LiDAR odometry, solid state LiDAR, continuous time, Gaussian mixture model

## I. INTRODUCTION

**L**IGHT detection and ranging (LiDAR) sensors can directly obtain the accurate range measurements in various scenarios by actively emitting the laser beams, which enables them to be the essential sensors for perception and navigation. Currently, the dominant LiDAR odometry approaches [1], [2], [3], [4], [5] make use of the multi-line mechanical spinning scanners due to their simplicity and success in many robotic applications.

With the prevalence of autonomous driving, nearly all Original Equipment Manufacturers (OEMs) plan to equip LiDARs on their flagship cars. However, the conventional multi-line spinning LiDAR cannot fulfill the massive deployment requirements on price, size and reliability. To this end, the solid-state LiDARs (SSLs) have been received a bit attentions in recent. Differently from the scanning patterns and field of view, it is difficult to directly employ the methods for the traditional spinning LiDARs to deal with SSLs odometry. This may lead to the inferior performance. In this letter, we focus our attention on Risley prism-based Livox LiDARs [6], which have the irregular scanning patterns and lower price at \$600.

The main difficulty in the prism-based SSL odometry is the sparsity of scanning pattern in a small FoV. As described in [6], the non-repetitive scanning technique for Livox Mid-40 requires 0.5s for integration to achieve the same vertical

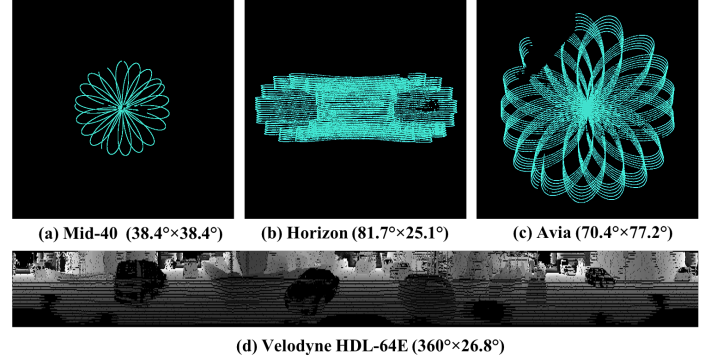


Fig. 1: Spherical projection results of different LiDARs within 0.1 second integration time. Compared to spinning LiDAR (d), the scanning patterns of SSL (a-c) are sparse with a small FoV.

coverage as 64-line Velodyne LiDAR. Moreover, its horizon angle is only  $38.4^\circ$  rather than  $360^\circ$  in the conventional spinning LiDAR. To facilitate the real-time applications, the output frequency of LiDAR odometry should be above 10 Hz. In contrast to the spinning LiDAR, the scattered points from SSLs integrated within the time window of 0.1s are too sparse, as shown in Fig. 1. It is hard to extract the useful features from them for scan registration. Therefore, the traditional LOAM-based method [1] is not very effective for SSLs odometry.

No matter what scanning mode it is, such as spinning, MEMS and prism, the common characteristic of LiDAR is that there are few points measured at the same time even with the advanced 128-line LiDAR. To enlarge the overlap between the consecutive scans, a set of 3D points are accumulated in a period of time to achieve better registration. Generally, we assume that all points are sampled at the beginning of this scan. Thus, motion distortions within a scan inevitably occur due to the sensor's movement, as shown in Fig. 3. It is similar to the rolling shutter effect in visual odometry [7]. A lot of previous LiDAR odometry methods [1], [2], [3], [8] compensate it by Inertial Measurement Unit (IMU), which is developed for the multi-line spinning LiDARs. However, there are very few approach to the SSLs odometry [9]. Most of SSLs only use single pair of semiconductor transceiver to make the device more compact. The single laser beam needs to change direction at high frequency by MEMS or prisms to cover a piece of area. Thus, these complicated scanning methods lead to more serious distortions.

To tackle the above critical challenges, we present an effective Continuous Time LiDAR Odometry (ECTLO) method for SSLs with the non-repetitive scanning patterns in this letter. Inspired by the recent progress on multi-line spinning

Xin Zheng and Jianke Zhu are with the College of Computer Science, Zhejiang University, Hangzhou, China, 310027.

E-mail: {xinzhen, jkzhu}@zju.edu.cn.

Jianke Zhu is the Corresponding Author.

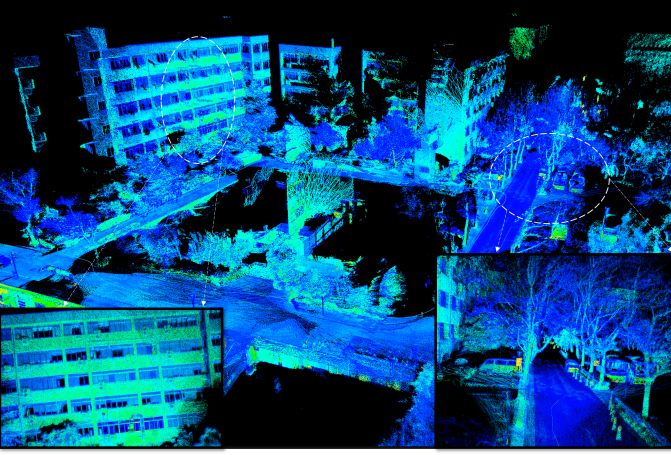


Fig. 2: Reconstruction results of our proposed approach on the data collected by Livox Mid-40. Two pictures at the bottom show details of structured facades and unstructured streets.

LiDAR [10], we try to eliminate the motion distortions within a scan through a continuous-time motion model. To account for the sparsity of a single scan, we take advantage of a point-to-plane Gaussian Mixture Model scheme [11] to effectively align the scans. Besides, we directly register raw points from LiDAR to avoid the complicated feature extraction for the diverse scanning patterns. As in [5], we maintain the map points through a range image so that the spatial relationship of points can be employed to efficiently speed up the scan registration. Fig 2 shows the example reconstruction results of our proposed approach.

In summary, the main contributions of this letter are: 1) an effective LiDAR odometry method for solid-state LiDAR by taking advantage of a continuous-time model to account for the motion distortions; 2) a novel robust filter registration scheme efficiently implemented on GPU to deal with the sparsity of scanning patterns; 3) extensive experiments on a series of challenging datasets demonstrate that our proposed approach outperforms the state-of-the-art LiDAR-only methods.

## II. RELATED WORK

Our proposed approach aims to deal with the challenge of SSLs odometry. In this section, we briefly review the most relevant studies on solid-state LiDAR odometry, motion compensation, and point set registration.

### A. Solid-state LiDAR Odometry

Despite that Solid-state LiDARs emerge as the promising range sensor in recent years, there are still few odometry approaches. Comparing to the conventional multi-line LiDARs with 360-degree coverage, these solid-state LiDARs have the sparse scanning patterns with small FoVs, which raises many issues on scan registration. Wang et al. [12] adapt LOAM [1] for a MEMS-based SSL (Intel L515) in indoor environment. Lin and Zhang [9] employ a prism-based SSL (Livox Mid-40) for outdoor scanning.

Due to the small FoV and low density of point cloud, the conventional methods cannot handle fast motion and jittering. To overcome the limitation of single sensor, Li et al. [13]

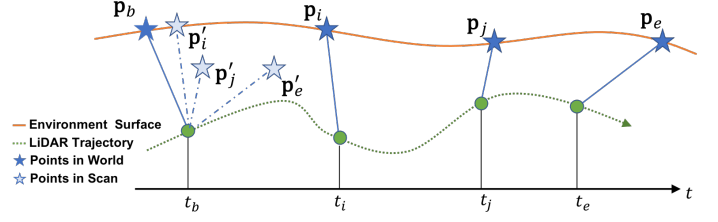


Fig. 3: Motion distortions in a scan  $t \in [t_b, t_e)$ . The sensor measurement is relative to the LiDAR center that moves along the trajectory. If all points are regarded as being sampled at  $t_b$ , the measurements are not the true position in world coordinate.

present a tightly-coupled LiDAR-inertial odometry framework for Livox Horizon. Moreover, Xu and Zhang [14] fuse multi-sensor information by an Iterated Extended Kalman Filter using Livox Avia. To achieve accurate registration, both of them rely on the additional sensor and LiDARs having more dense scanning pattern with large FoV.

### B. Motion Compensation

Motion distortions in LiDARs are mainly due to the continuous movement of laser beam, as shown in Fig. 3. To address this issue, a straightforward approach is to make use of the constant velocity motion model [1], [3], which undistorts the current point cloud with velocity from previous poses or extra IMU measurements. However, the constant velocity assumption may not be valid in real-world applications with fast orientation or position changes, especially for the handheld devices. Continuous-time model [8], [15] is more accurate to capture the motions by treating poses as a continuous-time trajectory. To account for fast motion, it requires a lot of control poses within a scan. The spline strictly constrains the continuity between control poses, which brings the extra cost in optimization. These drawbacks prohibit it from the real-time applications. Recently, Dellenbach et al. [10] compensate the distortions in conventional spinning LiDAR by linearly interpolating the beginning pose with end one within a scan, where the discontinuity between consecutive scans is penalized by the additional position and velocity constraints.

Generally, motion distortions are very serious in SSLs, which bring the extra difficulty for point registration. Lin and Zhang [9] segment single scan into several pieces to reduce the motion distortions. Xu and Zhang [14] de-skew points by the initial pose from IMU measurements. Both of them do not explicitly utilize the continuous-time model within the scan. To this end, we parameterize the pose through continuous-time model for SSLs, which is capable of undistorting the raw points within a scan without extra sensor.

### C. Point Set Registration

Generally, LiDAR odometry is treated as a point-set registration problem in literature. Given the input point clouds perceived by LiDAR at two consecutive timestamps, Iterative Closed Point (ICP) algorithm [16] is the typical solution to align them, which updates the relative transformation iteratively until convergence. LOAM [1] is the most successful LiDAR odometry approach, which selects the feature points by

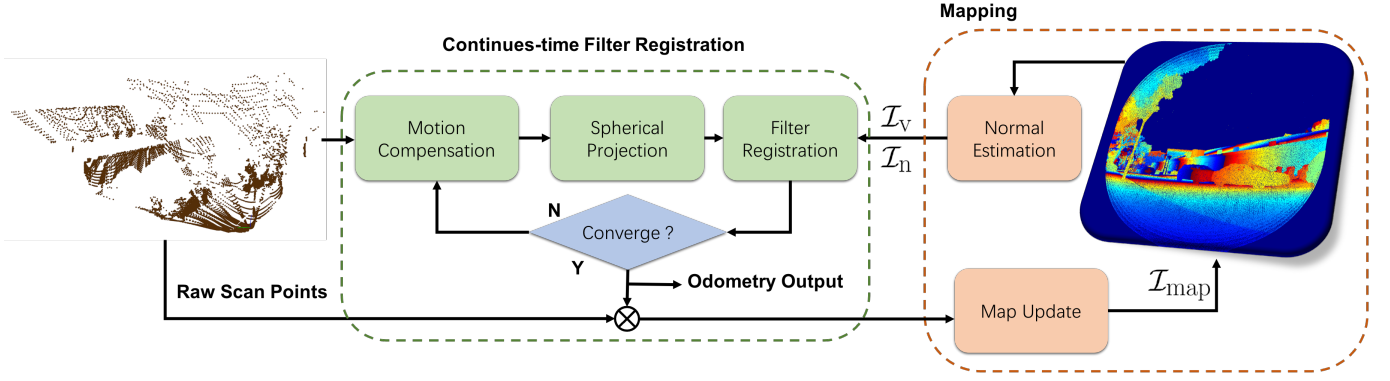


Fig. 4: Overview of our proposed ECTLO approach. Once the scan is obtained, the optimal state  $\mathbf{s} = [\mathbf{T}_{\text{WL}_b}, \mathbf{T}_{\text{WL}_e}]$  is predicted by continuous-time filter registration. The mapping module combines the input scan  $\mathcal{P}$  with the previous range map by the odometry result  $\mathbf{s}$  to form an updated range image  $\mathcal{I}_{\text{map}}$ .

computing the roughness of scattered points on each scan line. Moreover, a variant of ICP algorithm is employed to make use of both point-to-line [17] and point-to-plane loss [18], which achieves low-drift odometry with real-time performance.

The accuracy of ICP registration depends on the reliable correspondences between point sets, which is suspect to noise, outliers, and occlusions [19]. To this end, the probabilistic model is usually regarded as a more robust approach to align point sets. Generalized-ICP [20] formulates the point set registration problem into a probabilistic framework, which unifies point-to-point, point-to-plane and plane-to-plane ICP by covariance estimation. Similarly, Normal distribution transformation (NDT) [21] replaces the single point by normal distribution within a pre-defined regular voxel. These correlation-based registration methods can be interpreted as minimizing the distance between distributions.

Assuming that each point has a Gaussian variance, point cloud can be regarded as a Gaussian Mixture Model (GMM) [22], [19]. However, GMM-based methods are computationally intensive, which hinder them from real-time applications. Gao and Tedrake [11] present a probabilistic model, which computes filter-based correspondences in E step and updates pose by Gauss-Newton algorithm in M step. In this letter, we employ filter registration to tackle the SSLs odometry problem, in which the permutohedral filter is replaced by an efficient patch filter on range image [5].

### III. METHOD

In this section, we present the details of our proposed SSLs odometry approach. Firstly, LiDAR odometry is formulated into a robust GMM-based probabilistic registration problem on range image. Then, we suggest a continuous-time model to compensate the severe motion distortions in SSLs, which has the effective analytic Jacobian for optimization. Finally, we give the details of mapping scheme. Fig. 4 shows the overview of our method.

#### A. Preliminary

Assume that the point measurement is relative to LiDAR coordinate system  $\mathcal{L}_t$  at timestamp  $t$ . We denote the orientation and position of LiDAR as  $\mathbf{T}_{\text{WL}_t}$  with respect to the world frame  $\mathcal{W}$  at timestamp  $t$ , where the world frame is  $\mathcal{W} = \mathcal{L}_0$  at the starting location.

In this letter, the movement of LiDAR is in special Euclidean space. To obtain an unconstrained minimization problem, we apply the twist parameterization from Lie Algebra[23], where a vector  $\boldsymbol{\xi} \in \mathbb{R}^6$  represents rigid transformation  $\mathbf{T}_{\text{WL}} \in \text{SE}(3)$ . All operators are right-version as below

$$\begin{aligned} \text{right-}\oplus : \mathcal{Y} &= \mathcal{X} \oplus \boldsymbol{\xi} = \mathcal{X} \text{Exp}(\boldsymbol{\xi}) \in \text{SE}(3) \\ \text{right-}\ominus : \boldsymbol{\xi} &= \mathcal{Y} \ominus \mathcal{X} = \text{Log}(\mathcal{X}^{-1}\mathcal{Y}) \in \mathbb{R}^6. \end{aligned} \quad (1)$$

where  $\mathcal{X}, \mathcal{Y} \in \text{SE}(3)$ .  $\text{Log}(\cdot) : \text{SE}(3) \mapsto \mathbb{R}^6$  is the logarithmic mapping, and  $\text{Exp}(\cdot) : \mathbb{R}^6 \mapsto \text{SE}(3)$  is the inverse exponential mapping.

#### B. Filter Registration for LiDAR Odometry

Comparing to the spinning LiDAR, the scanning pattern of prism-based SSLs is very sparse in a small integration period, as illustrated in Fig. 1. Therefore, the conventional registration methods like ICP and its variants [1], [9], [4] may not be effective for SSLs odometry. To this end, we adopt a probabilistic method, which is more robust to noise, outliers, and occlusions. Besides, a Gaussian filtering algorithm is employed to efficiently find the correspondences in 2D range image.

1) *Probabilistic Formulation*: The fundamental problem of LiDAR odometry is to find a series of discrete motion parameters properly describing the LiDAR movement. Once the raw scan  $\mathcal{P}$  is obtained, the transformation between the current scan  $\mathcal{P}$  and previous map  $\mathcal{Q}$ .  $\mathbf{p}_1, \mathbf{p}_2, \dots, \mathbf{p}_M$  is estimated.  $\mathbf{q}_1, \mathbf{q}_2, \dots, \mathbf{q}_N$  are points in  $\mathcal{P}$  and  $\mathcal{Q}$ , respectively.

Under the framework of GMM-based probabilistic registration [19], [11], [24], aligning one source point set to another fixed target is formulated as a Maximum Likelihood Estimation (MLE) problem. Like the factorization scheme in FilterReg [11], the local map  $\mathcal{Q}$  is fixed while the scan  $\mathcal{P}$  is changing its position controlled by the motion parameter  $\mathbf{s}$  in order to align with  $\mathcal{Q}$ . GMMs in our method is built from the local map  $\mathcal{Q}$ .

Given the source point set  $\mathcal{P}$  and target  $\mathcal{Q}$  independent on  $\mathbf{s}$ , we aim to maximize the joint distribution as below

$$p(\mathcal{P}, \mathcal{Q}, \mathbf{s}) \propto \phi_{\text{kinematic}}(\mathcal{P}, \mathbf{s}) \phi_{\text{geometric}}(\mathcal{P}, \mathcal{Q}), \quad (2)$$

where  $\phi_{\text{geometric}}(\mathcal{P}, \mathcal{Q})$  is the potential function that captures the geometric relationship.  $\phi_{\text{kinematic}}(\mathcal{P}, \mathbf{s})$  encodes the kinematic model. For simplicity, its derivation is denoted as  $\mathbf{p}_i(\mathbf{s})$ .

If the kinematic model  $\phi_{\text{kinematic}}(\mathcal{P}, \mathbf{s})$  is already captured, the joint distribution  $p(\mathbf{p}_i, \mathbf{s} \mid \mathcal{Q})$  of each scan point can be a GMM as below

$$w_i p_o(\mathbf{p}_i) + (1 - w_i) \sum_{j=1}^J \pi(\mathbf{q}_j) p(\mathbf{p}_i(\mathbf{s}) \mid \mathbf{q}_j), \quad (3)$$

where  $p(\mathbf{p}_i(\mathbf{s}) \mid \mathbf{q}_j) = \mathcal{N}(\mathbf{p}_i(\mathbf{s}); \mathbf{q}_j, \Sigma_{xyz})$  is the probability density function of Gaussian distribution.  $\mathbf{q}_j$  is the Gaussian centroid, and  $\Sigma_{xyz} = \text{diag}(\sigma_x^2, \sigma_y^2, \sigma_z^2)$  is the diagonal covariance matrix. The additional uniform distribution  $p_o(\mathbf{p}_i) = \frac{1}{M}$  is added to account for outliers.  $w_i \in [0, 1]$  is the weight of  $\mathbf{p}_i$ . Practically, it is inefficient to use all map points. Thus, we select the neighborhood points of  $\mathbf{p}_i(\mathbf{s})$  for approximation. Each GMM component of map point has equal probabilities  $\pi(\mathbf{q}_j) = \frac{1}{J}$ , where  $J$  is the size of valid neighborhoods.

Each point in scan  $\mathcal{P}$  is conditional independent on  $\mathbf{s}$ . We aim to find the optimal state  $\mathbf{s}$  that maximizes the log-likelihood function as follows

$$L(\mathbf{s}) = \log(p(\mathcal{P}, \mathcal{Q}, \mathbf{s})) = \sum_{i=1}^M \log(p(\mathbf{p}_i, \mathbf{s} \mid \mathcal{Q})). \quad (4)$$

Since it is hard to directly solve the above optimization, the EM algorithm is employed to iteratively find its solution. The data association between scan points and local map is implicitly reflected by the latent variable. As in [11], we estimate the motion parameter  $\mathbf{s}$  by EM algorithm with more reliable point-to-plane criteria in the following.

**E step:** for each point in scan  $\mathcal{P}$ , compute

$$\begin{aligned} \mathbf{m}_{\mathbf{p}_i}^0 &= \sum_{\mathbf{q}_j} \mathcal{N}(\mathbf{p}_i(\mathbf{s}^{\text{old}}); \mathbf{q}_j, \Sigma_{xyz}) \\ \mathbf{m}_{\mathbf{p}_i}^1 &= \sum_{\mathbf{q}_j} \mathcal{N}(\mathbf{p}_i(\mathbf{s}^{\text{old}}); \mathbf{q}_j, \Sigma_{xyz}) \mathbf{q}_j \\ \mathbf{n}_{\mathbf{p}_i} &= (\sum_{\mathbf{q}_j} \mathcal{N}(\mathbf{p}_i(\mathbf{s}^{\text{old}}); \mathbf{q}_j, \Sigma_{xyz}) \mathbf{n}_{\mathbf{q}_j}) / \mathbf{m}_{\mathbf{p}_i}^0 \end{aligned} \quad (5)$$

**M step:** minimize the following objective function

$$E_{\text{reg}}(\mathbf{s}) = \frac{1}{M} \sum_{\mathbf{p}_i} \frac{\mathbf{m}_{\mathbf{p}_i}^0}{\mathbf{m}_{\mathbf{p}_i}^0 + c} \text{dot} \left( \mathbf{n}_{\mathbf{p}_i}, \mathbf{p}_i(\mathbf{s}) - \frac{\mathbf{m}_{\mathbf{p}_i}^1}{\mathbf{m}_{\mathbf{p}_i}^0} \right)^2 \quad (6)$$

where  $c = \frac{w_i}{1-w_i} \frac{J}{M}$ .

2) *Filter-based Correspondence on Range Image:* Just like the closet point searching in ICP, the E step is to compute the correspondence of scan point  $\mathbf{p}_i$ . The form of  $\mathbf{m}_{\mathbf{p}_i}^0, \mathbf{m}_{\mathbf{p}_i}^1, \mathbf{n}_{\mathbf{p}_i}$  are Gaussian Transform. Obviously, the bottleneck of this EM algorithm is how to efficiently compute thousands of the above independent items in E step. FilterReg [11] uses a customized permutohedral lattice filter to facilitate the efficient computation while retaining the sufficient accuracy. In this letter, we consider the point registration problem in 3D space rather than the general N-dimensional space. Therefore, an efficient 2D Gaussian filter is used by taking advantage on range image representation.

In contrast to KD-Tree [1], [2] and voxel [21], the range image is not only a low memory consumption but also computational efficient data structural. We extend this representation from conventional multi-line spinning LiDARs [5] to SSLs. A

range image is an index table  $\mathcal{I} : \mathbb{R}^2 \mapsto \mathbb{R}^3$  that reserves the spatial relationship of 3D point set within single 2D image. Given a point  $(x, y, z)^\top$  relative to range image origin, its correspondence can be indexed in previous image by spherical projection  $\Pi : \mathbb{R}^3 \mapsto \mathbb{R}^2$

$$\begin{bmatrix} u \\ v \end{bmatrix} = \Pi(x, y, z) = \begin{bmatrix} (1/2 + \arctan(y/x) \cdot f_{hor}^{-1}) w \\ (1/2 - \arcsin(z/r) \cdot f_{ver}^{-1}) h \end{bmatrix}, \quad (7)$$

where  $r = \sqrt{x^2 + y^2 + z^2}$ .  $w$  and  $h$  are the width and height of image. The pixel length of  $w$  and  $h$  is proportion to angular resolution  $\beta_{\text{res}}$  and FoV. The major difference between SSLs and spinning LiDAR is the limited FoV on horizontal view, which is  $38.4^\circ$  for Livox Mid-40 and  $81.7^\circ$  for Livox Horizon comparing to  $360^\circ$  for spinning LiDAR. Note that  $f_{hor}$  and  $f_{ver}$  are user-defined FoV rather than the original LiDAR sensor's, which keeps the abundant historical points out of SSLs' FoV to facilitate robust registration.

The generation of initial range image  $\mathcal{I}_{\text{map}}$  and updating scheme are described in Sec. III-D. During scan registration, map points  $\mathcal{Q}$  are fixed so that their normal vectors do not change. By making use of point-to-plane criteria, we convert the previous map  $\mathcal{I}_{\text{map}}$  into two temporal index tables, vertex map  $\mathcal{I}_v$  storing 3D position information, and normal map  $\mathcal{I}_n$  saving their normal vector. The valid planar points are selected by choosing those surface curvatures are below the threshold  $\delta_\sigma$ . We flip the normal direction when the angle between normal vector and point is larger than  $90^\circ$ . Note that we only need to calculate normal once before EM procedure.

The advantage of range image is to retain the 3D spatial relationship within a 2D index table, where its neighbor exists in adjacent pixels. Therefore, the Gaussian Transform can be efficiently computed by image filter methods like Gaussian Blur or Bilateral Filter. Practically, those points far away from  $\mathbf{p}_i$  have a small probability density, which may not affect the final result. Thus, we only consider neighborhoods of point  $\mathbf{p}_i$  for approximation. If the spherical projection result of  $\mathbf{p}_i$  is  $(u_i, v_i)$ , the related map points affecting the correspondence are in adjacent pixels. Hereby, Gaussian filter are employed in a pre-defined window  $\mathcal{W}_i$  with center  $(u_i, v_i)$  to compute the filter-based correspondence. By taking advantage of range image representation, the filter can be efficiently implemented on GPU, where each kernel processes a single scan point.

### C. Continuous-time Filter Registration

The total number of laser transceivers are limited in modern commercial LiDARs in order to reduce the size of equipment. Thus, we name the point set as scan for better registration, which is the accumulated point cloud during a period of time  $t \in [t_b, t_e]$ .  $t_b$  is beginning time-stamp of the scan, and  $t_e$  is end timestamp. Motion distortion occurs when treating all points sampled simultaneously. To deal with it, we employ a continuous-time model to compensate the motion distortions in filter registration.

The kinematic model of LiDAR within a scan  $\phi_{\text{kinematic}}(\mathcal{P}, \mathbf{s})$  is parameterized by two controlled poses, including the beginning of scan  $\mathbf{T}_{\text{WL}_b}$  and end of scan  $\mathbf{T}_{\text{WL}_e}$ . The estimation target is the state  $\mathbf{s} = [\mathbf{T}_{\text{WL}_b}, \mathbf{T}_{\text{WL}_e}]$ , where  $\mathbf{s}$  is in  $\mathbb{R}^{12}$  through the minimal representation of Lie algebra.



1) *Motion Compensation*: To compensate the motion distortions, the points within a scan are transformed into the world coordinate via linear interpolation on SE(3). Given a raw point measurement  $\mathbf{p}_i \in \mathbb{R}^3$  at timestamp  $t_i \in [t_b, t_e]$ , its corrected position  $\mathbf{p}_i(\mathbf{s})$  in world coordinate is computed by

$$\begin{aligned}\boldsymbol{\tau} &= \mathbf{T}_{\text{WL}_e} \ominus \mathbf{T}_{\text{WL}_b} \\ \alpha &= (t_i - t_b)/(t_e - t_b) \\ \mathbf{T}_{\text{WL}_i} &= \mathbf{T}_{\text{WL}_b} \text{Exp}(\alpha \boldsymbol{\tau}) \\ \mathbf{p}_i(\mathbf{s}) &= \mathbf{T}_{\text{WL}_i} \mathbf{p}_i\end{aligned}\quad (8)$$

where  $\boldsymbol{\tau} \in \mathbb{R}^6$  is the tangent space of manifold SE(3), and  $\mathbf{T}_{\text{WL}_i}$  is the LiDAR origin at timestamp  $t_i$  in world coordinate. Each 3D point  $(x, y, z)^\top$  is represented in homogeneous coordinates as  $\mathbf{p}_i = (x, y, z, 1)^\top$ . As the estimated state  $\mathbf{s}$  is updated iteratively until the convergence, point  $\mathbf{p}_i(\mathbf{s})$  is recomputed with the newly updated pose at each iteration.

Generally, the output frequency of conventional spinning LiDAR is 10 Hz for self-driving cars that move steadily. This is usually regarded as uniform motion. In the case of rapid motion, the approximation of linear interpolation on SE(3) may not be valid. Specifically, handheld or air-borne devices are shakier, whose rotation change may exceed  $90^\circ$  instantly. This breaks the precondition of linear interpolation. Thus, nearly all LiDAR-only methods fail in such circumstance without the help from IMU. Fortunately, the output frequency of LiDAR packet is up to 1000 Hz so that we can reduce the integration time for better motion compensation. The duration of integration time needs to balance the registration robustness and computational cost.

2) *Motion Constraints*: We employ the beginning pose and end state of a scan to parameterize the movement within its interval. With the continuous-time trajectory, the beginning pose of current scan should be consistent with end pose of previous one. Thus, the new state is initialized by its previous pose as follows

$$\begin{aligned}\mathbf{T}_{\text{WL}_b}^n &= \mathbf{T}_{\text{WL}_e}^{n-1} \\ \mathbf{T}_{\text{WL}_e}^n &= \mathbf{T}_{\text{WL}_b}^n (\mathbf{T}_{\text{WL}_b}^{n-1})^{-1} \mathbf{T}_{\text{WL}_e}^{n-1},\end{aligned}\quad (9)$$

where the first state  $\mathbf{s}_0$  is set to identity.

The previous method [10] only takes into account of the translation consistency between the consecutive scans in self-driving cars. However, the movement of handheld devices is more complicated and irregular, where the orientation change needs to be considered as well. In this letter, we directly penalize the continuity of rotation and translation in SE(3) space. Therefore, we impose the location consistency constraint  $E_{\text{loc}}$  as below

$$E_{\text{loc}}(\mathbf{s}) = \mathbf{r}_{\text{loc}}^\top \mathbf{r}_{\text{loc}}, \quad (10)$$

where the position difference is defined as  $\mathbf{r}_{\text{loc}} = \mathbf{T}_{\text{WL}_b}^n \ominus \mathbf{T}_{\text{WL}_e}^{n-1}$ .

To take into account of the motion smoothness, we impose the constant velocity constraint  $E_{\text{vel}}$  that is defined as follows

$$E_{\text{vel}}(\mathbf{s}) = \mathbf{r}_{\text{vel}}^\top \mathbf{r}_{\text{vel}}, \quad (11)$$

where the velocity difference between the consecutive scans is computed by

$$\mathbf{r}_{\text{vel}} = (\mathbf{T}_{\text{WL}_e}^n \ominus \mathbf{T}_{\text{WL}_b}^n) - (\mathbf{T}_{\text{WL}_e}^{n-1} \ominus \mathbf{T}_{\text{WL}_b}^{n-1}). \quad (12)$$

With the above proposed motion constraints, we reformulate the previous M step in Eqn. 6 into a continuous-time form,

$$E_{\text{ct-reg}}(\mathbf{s}) = E_{\text{reg}}(\mathbf{s}) + \lambda_l E_{\text{loc}}(\mathbf{s}) + \lambda_v E_{\text{vel}}(\mathbf{s}), \quad (13)$$

where  $\lambda_l$  and  $\lambda_v$  are two regularization coefficients to balance the above energy terms.

3) *Gauss-Newton in EM Procedure*: The optimization in M step is a least square minimization problem, which can be reformulated into the generalized form  $\sum c_i \mathbf{r}_i^\top \mathbf{r}_i$ .  $c_i$  is the weight coefficient, and  $\mathbf{r}_i$  is the residual of energy term. In our proposed SSLs odometry approach, there are three kinds of residual, including  $\mathbf{r}_{\text{reg}}^i = \mathbf{n}_{\mathbf{p}_i}^\top (\mathbf{p}_i(\mathbf{s}) - \mathbf{m}_{\mathbf{p}_i}^1 / \mathbf{m}_{\mathbf{p}_i}^0)$ ,  $\mathbf{r}_{\text{loc}}$  and  $\mathbf{r}_{\text{vel}}$ . By the first order Taylor expansion, the residual around  $\mathbf{s}$  is approximated as follows

$$\mathbf{r}_i(\mathbf{s} + \Delta \mathbf{s}) \simeq \mathbf{r}_i(\mathbf{s}) + \frac{\partial \mathbf{r}_i}{\partial \mathbf{s}} \Delta \mathbf{s}, \quad (14)$$

where  $\frac{\partial \mathbf{r}_i}{\partial \mathbf{s}}$  is the Jacobian, and  $\Delta \mathbf{s} = [\Delta \boldsymbol{\xi}_b \ \Delta \boldsymbol{\xi}_e]$  is the increment. In Gauss-Newton (GN) algorithm, the optimal increment minimizing  $E_{\text{ct-reg}}(\mathbf{s})$  is found by solving the linear equation  $\mathbf{H} \Delta \mathbf{s} = -\mathbf{b}$ , where the Hessian matrix  $\mathbf{H} = \sum c_i \left( \frac{\partial \mathbf{r}_i}{\partial \mathbf{s}} \right)^\top \frac{\partial \mathbf{r}_i}{\partial \mathbf{s}}$  and  $\mathbf{b} = \sum c_i \left( \frac{\partial \mathbf{r}_i}{\partial \mathbf{s}} \right)^\top \mathbf{r}_i$ . The concrete form of odometry can be derived as below

$$\begin{aligned}\mathbf{H} &= \frac{1}{M} \sum_{\mathbf{p}_i} \frac{\mathbf{m}_{\mathbf{p}_i}^0}{\mathbf{m}_{\mathbf{p}_i}^0 + c} \left( \frac{\partial \mathbf{r}_{\text{reg}}^i}{\partial \mathbf{s}} \right)^\top \frac{\partial \mathbf{r}_{\text{reg}}^i}{\partial \mathbf{s}} \\ &\quad + \lambda_l \left( \frac{\partial \mathbf{r}_{\text{loc}}}{\partial \mathbf{s}} \right)^\top \frac{\partial \mathbf{r}_{\text{loc}}}{\partial \mathbf{s}} + \lambda_v \left( \frac{\partial \mathbf{r}_{\text{vel}}}{\partial \mathbf{s}} \right)^\top \frac{\partial \mathbf{r}_{\text{vel}}}{\partial \mathbf{s}} \\ \mathbf{b} &= \frac{1}{M} \sum_{\mathbf{p}_i} \frac{\mathbf{m}_{\mathbf{p}_i}^0}{\mathbf{m}_{\mathbf{p}_i}^0 + c} \left( \frac{\partial \mathbf{r}_{\text{reg}}^i}{\partial \mathbf{s}} \right)^\top \mathbf{r}_{\text{reg}}^i \\ &\quad + \lambda_l \left( \frac{\partial \mathbf{r}_{\text{loc}}}{\partial \mathbf{s}} \right)^\top \mathbf{r}_{\text{loc}} + \lambda_v \left( \frac{\partial \mathbf{r}_{\text{vel}}}{\partial \mathbf{s}} \right)^\top \mathbf{r}_{\text{vel}}.\end{aligned}\quad (15)$$

Since  $\mathbf{T}_{\text{WL}_b}$  and  $\mathbf{T}_{\text{WL}_e}$  are represented in SE(3), the new state  $\mathbf{s}$  for the next E step is updated through  $\mathbf{s} = \mathbf{s}^{\text{old}} \oplus \Delta \mathbf{s}$ . Specifically, the two poses are updated as follows

$$\mathbf{T}_{\text{WL}_b} \leftarrow \mathbf{T}_{\text{WL}_b} \oplus \Delta \boldsymbol{\xi}_b, \mathbf{T}_{\text{WL}_e} \leftarrow \mathbf{T}_{\text{WL}_e} \oplus \Delta \boldsymbol{\xi}_e. \quad (16)$$

The computational cost in M step is mainly dominated in calculating the Jacobian. To this end, we derive the analytic Jacobians of each residual with respect to the beginning pose  $\mathbf{T}_{\text{WL}_b}$  and the end pose  $\mathbf{T}_{\text{WL}_e}$  for efficient optimization. The analytic Jacobian of registration term is computed by

$$\begin{aligned}\frac{\partial \mathbf{r}_{\text{reg}}^i}{\partial \mathbf{s}} &= \mathbf{n}_{\mathbf{p}_i}^\top \frac{\partial (\mathbf{T}_{\text{WL}_i} \mathbf{p}_i)}{\partial \mathbf{T}_{\text{WL}_i}} \begin{bmatrix} \frac{\partial \mathbf{T}_{\text{WL}_i}}{\partial \mathbf{T}_{\text{WL}_b}} & \frac{\partial \mathbf{T}_{\text{WL}_i}}{\partial \mathbf{T}_{\text{WL}_e}} \end{bmatrix} \\ \frac{\partial (\mathbf{T}_{\text{WL}_i} \mathbf{p}_i)}{\partial \mathbf{T}_{\text{WL}_i}} &= [\mathbf{R}_{\text{WL}_i} \quad -\mathbf{R}_{\text{WL}_i} [\mathbf{p}_i]_\times] \\ \frac{\partial \mathbf{T}_{\text{WL}_i}}{\partial \mathbf{T}_{\text{WL}_b}} &= (1 - \alpha) \mathbf{J}_r ((\alpha - 1) \boldsymbol{\tau}) \mathbf{J}_l^{-1}(\boldsymbol{\tau}) \\ \frac{\partial \mathbf{T}_{\text{WL}_i}}{\partial \mathbf{T}_{\text{WL}_e}} &= \alpha \mathbf{J}_r(\alpha \boldsymbol{\tau}) \mathbf{J}_r^{-1}(\boldsymbol{\tau}),\end{aligned}\quad (17)$$

As in [23],  $\mathbf{J}_r(\cdot)$  and  $\mathbf{J}_l(\cdot)$  are the right- and left- Jacobians, respectively.  $[\cdot]_\times$  denotes the skew symmetric matrix.

Similarly, the analytic Jacobians of motion constraints can be derived as below

$$\begin{aligned} \frac{\partial \mathbf{r}_{\text{loc}}}{\partial \mathbf{s}} &= [\mathbf{J}_r^{-1}(\mathbf{r}_{\text{loc}}) \quad \mathbf{0}] \\ \frac{\partial \mathbf{r}_{\text{vel}}}{\partial \mathbf{s}} &= [-\mathbf{J}_l^{-1}(\boldsymbol{\tau}) \quad \mathbf{J}_r^{-1}(\boldsymbol{\tau})]. \end{aligned} \quad (18)$$

#### D. Mapping

To enlarge the overlap between scan and map, we suggest a scan-to-map scheme that makes full use of the historical information. As shown in Fig. 4, we only maintain single range image  $\mathcal{I}_{\text{map}}$  in global memory to retain the history map points. In EM procedure, there are two temporal image  $\mathcal{I}_v$  and  $\mathcal{I}_n$  for efficient data association, which are pre-computed by normal estimation [5]. The memory consumption of map points is dependent on the size of range image. Therefore, it is fixed when the parameters like FoV and angular resolution are determined.

Our presented mapping scheme is simple yet effective. At the beginning, we initialize  $\mathcal{I}_{\text{map}}$  by projecting several scans onto the blank range image. If the projected pixel is occupied, we keep the point close to local LiDAR origin. At the initial state, this origin is the starting position of LiDAR. After a successful registration, we change the origin to the beginning pose of current scan, and generate a new  $\mathcal{I}_{\text{map}}$  for the next EM optimization. The map updating scheme is introduced in the following. Firstly, all points with respect to last origin  $\mathbf{T}_{\text{WL}_b}^{\text{old}}$  in the previous range image are transferred to the current map origin  $\mathbf{T}_{\text{WL}_b}$  to generate a new  $\mathcal{I}_{\text{map}}$ . Secondly, we adjust the point position within current scan by motion compensation, which are further projected onto  $\mathcal{I}_{\text{map}}$  to update local map. Finally, the collision is resolved by selecting the nearest point similar to the initialization.

### IV. EXPERIMENT

In this section, we present the details of our experiments and discuss the results of LiDAR odometry. We evaluate our proposed approach on several datasets collected by various SSLs with different scanning patterns. The effectiveness of continuous-time model and filter registration are investigated in ablation study. Additionally, we present the efficiency analysis on both commodity laptop and the embedded devices.

#### A. Experimental Testbed

Our method is implemented in C++ with CUDA. The experiments are performed on a laptop computer with an Intel Core i7-9750H CPU@2.60 GHz having 16GB RAM and an NVIDIA GeForce RTX 2060 GPU. Additionally, we evaluate the computational time of our proposed approach on NVIDIA Jetson Nano and AGX, which are the popular embedded devices in robotics. For simplicity, we name our method as ECTLO. Table I gives the parameter settings.

To examine the effectiveness of our presented method, the experiments have been conducted on three different SSLs. The first LiDAR is Livox Mid-40 that has a circular FoV

TABLE I: Parameter Settings of Our Method

Parameter	value	Parameter	value
$f_{\text{hor}}, f_{\text{ver}}$ (Livox Mid-40)	50°, 50°	$\lambda_l, \lambda_v$	0.1, 0.1
$f_{\text{hor}}, f_{\text{ver}}$ (Livox Horizon)	90°, 30°	$\sigma_x, \sigma_y, \sigma_z$	0.25
$f_{\text{hor}}, f_{\text{ver}}$ (Livox Avia)	80°, 80°	$w_i$	0.2
$\mathcal{W}_i$	7 × 7	$\beta_{\text{res}}$	10 pixels/o
$\delta_\sigma$	0.055		

of 38.4°. The second is Livox Horizon with 81.7° (horizon) × 25.1° (vertical) FoV. The third is Livox Avia whose FoV is 70.4° (horizon) × 77.2° (vertical). The testing data consists of two public datasets from the previous studies [9], [25], and one dataset collected by ourselves at Yuquan Campus, Zhejiang University.

#### B. Performance Evaluation

We compare our presented ECTLO method against the state-of-the-art approaches with publicly available implementations, including LOAM-Livox [9]<sup>1</sup>, BALM [26]<sup>2</sup>, and Livox-mapping<sup>3</sup>. Since all three datasets do not have the accurate groundtruth to validate the resulting trajectory, we compute the end-to-end distance by selecting those sequences with the same beginning and end positions. As the end-to-end position error is employed as the evaluation criterion, the loop closure module in LOAM-Livox is disabled for the sake of fair comparison.

Table II shows the quantitative results on the three datasets. It can be clearly seen that our proposed ECTLO approach achieves the lowest end-to-end position error comparing to other LiDAR only approaches. Since most of sequences are collected in outdoor environment having many trees and large open areas, BALM failed in most of cases except for indoor sequence ZJU-H1. This is because BALM is mainly designed for the structured scenarios.

For better illustration, we plot the trajectories and reconstruction results on the sequences of hku\_main and hku\_zym in Fig. 5. It can be clearly seen that our proposed ECTLO approach achieves the lowest drift even without the extra loop closure module, which obtains the high reconstruction quality by taking advantage of the accurate continuous-time filter registration. Livox-mapping is the official odometry package from Livox, however, its mapping result has obvious drifts. When the loop closure module in LOAM-Livox is enabled, the green line shows the corrected trajectory after loop closure, which is far away from the red line without correction.

To examine the gap between LiDAR-only odometry and sensor fusion methods, we compare our proposed LiDAR only approach against the state-of-the-art LiDAR-inertial odometry FAST-LIO [14]. It can be observed that our method achieves the comparable results in contrast to FAST-LIO<sup>4</sup>. Moreover, we plot the mapping result in Fig. 6. It is worthy of mentioning that our approach only uses the single sensor, which is able to achieve the high quality of reconstruction in large-scale outdoor environment with rapid motions.

<sup>1</sup>[https://github.com/hku-mars/loam\\_livox](https://github.com/hku-mars/loam_livox)

<sup>2</sup><https://github.com/hku-mars/BALM>

<sup>3</sup>[https://github.com/Livox-SDK/livox\\_mapping](https://github.com/Livox-SDK/livox_mapping)

<sup>4</sup>[https://github.com/hku-mars/FAST\\_LIO](https://github.com/hku-mars/FAST_LIO)

TABLE II: Quantitative Results of End-to-end Errors (meters) on Three Datasets

	Livox Mid-40				Livox Horizon		Livox Avia			
	loop_hku _main (389m)	loop_hku _zym (290m)	ZJU -M0 (296m)	ZJU -M1 (440m)	ZJU -H0 (651.3m)	ZJU -H1 (75.8m)	hku_campus _seq_00 (190.6m)	hku_ park_00 (247.3m)	hkust_campus _seq_00 (1317m)	hkust_campus _seq_01 (1524m)
Ours	2.40	0.62	1.72	1.73	2.73	0.29	0.25	0.60	8.63	4.72
LOAM_Livox [9]	8.50	6.90	7.21	5.61	— <sup>1</sup>	—	—	—	—	—
BALM [26]	×	×	×	×	×	0.36	×	×	×	×
Livox_mapping	24.45	14.69	11.45	14.25	26.90	2.81	0.10	3.44	620.86	296.96
FAST-LIO2 [14]	— <sup>1</sup>	—	—	—	0.04	7.22	0.07	0.96	4.91	0.31

<sup>1</sup> — Unavailable in this sequence. LOAM\_Livox is only designed for Livox Mid-40, and FAST-LIO2 needs the additional IMU measurements.

<sup>2</sup> × denotes that the method fails to obtain the results.

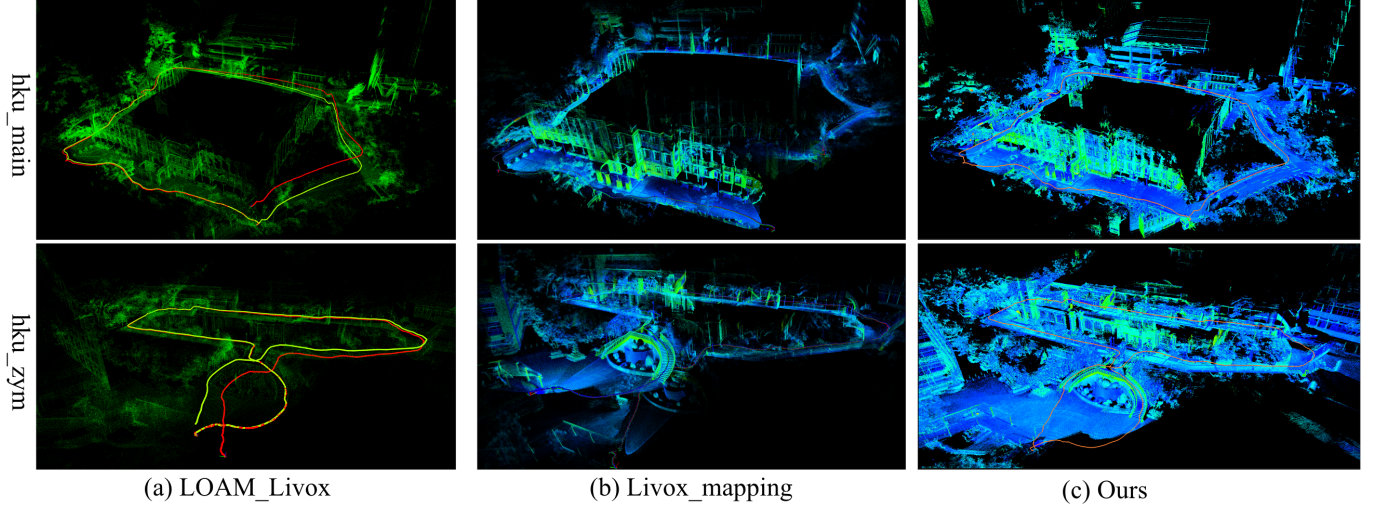


Fig. 5: The trajectory and reconstruction result of different methods on public Livox Mid-40 dataset. The green line in (a) is the trajectory with an extra loop closure module. The red line indicates the result without loop closure.

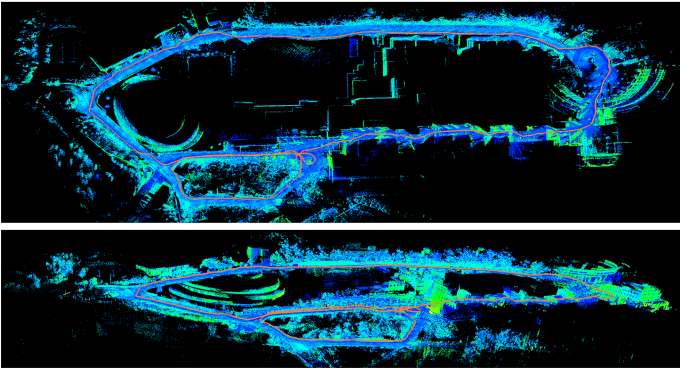


Fig. 6: The mapping result on large scale outdoor sequence hku\_campus\_01.

### C. Ablation Study

The main contributions of our proposed method are continuous-time model for motion compensation and GMM-based filter registration for LiDAR odometry. To investigate the effectiveness of each module, we conduct an ablation study with various settings. The experiments are performed on three sequences with different scanning patterns, including ZJU-M0, ZJU-H0 and hku\_park\_00. Table III shows the end-

TABLE III: Ablation Study on Our Proposed Approach.

CT Module	GMM Registration	End-to-end Error (m)		
		ZJU-M0	ZJU-H0	hku_park_00
×	×	×	×	37.02
×	✓	6.74	17.33	24.95
✓	×	0.53	44.33	0.38
✓	✓	0.77	2.52	0.32

<sup>1</sup> Without continuous-time motion model.

<sup>2</sup> Using point-to-plane ICP in [5] for registration.

to-end errors of different combinations. It can be observed that the continuous-time filter registration can significantly improve the odometry accuracy. Although continuous time module performs well on the easy sequences like ZJU-M0 and hku\_park\_00, it fails on the challenging ZJU-H0 sequence. Therefore, both continuous-time and GMM-based registration are essential to achieving the robust and accurate odometry results in various scenarios.

### D. Evaluation on Computational Efficiency

The computational load of our approach is mainly dominated by normal estimation and filter registration. By taking advantage of the range image representation, the spatial rela-

TABLE IV: Evaluation on Computational Time (ms)

	Dataset	Data Upload	Normal Estimation	Filter Registration	Map Updating	Total Time
Nano	ZJU-M0	0.97	21.53	25.45	10.38	58.33
	ZJU-H0	1.81	39.73	65.15	16.64	123.33
	ZJU-A0	2.07	86.76	50.96	38.65	178.44
AGX	ZJU-M0	0.36	2.36	4.46	1.87	9.05
	ZJU-H0	0.53	4.50	9.33	3.12	17.48
	ZJU-A0	0.57	9.23	7.72	4.75	22.27
Laptop	ZJU-M0	0.10	0.51	1.02	0.45	2.08
	ZJU-H0	0.19	1.04	2.73	0.77	4.73
	ZJU-A0	0.23	2.19	2.17	1.08	5.67

tionship among points can be used to speed up the millions of latent data associations. To demonstrate the efficiency of our presented method, we evaluate the computational costs at different stages, including data upload from CPU to GPU, normal estimation, filter registration, and map updating. Once the input point cloud is transferred to GPU memory, all the remaining steps are computed on GPU using CUDA. Additionally, we deploy our approach into the embedded devices from the entry-level NVIDIA Jetson Nano to the high-end Jetson AGX.

The computational time is highly affected by the total number of scattered points within a scan. For fair comparison, we set the output frequency of each SSLs to 10 Hz. Therefore, the total number of points in single scan is 10K for Livox Mid-40, and 24K for Livox Horizon and Avia. All the raw points are used without downsampling. As depicted in Table IV, our proposed approach runs around 480 fps on the commodity laptop, 110 fps on Jetson AGX, and 17 fps on Jetson Nano.

## V. CONCLUSION

This paper proposed an effective continuous-time filter registration approach to solid-state LiDAR odometry. We made use of the continuous-time model to compensate the motion distortions in SSLs. Moreover, GMM-based filter registration was employed to robustly align sparse point clouds with small FoV. Additionally, we employed the efficient range image representation, which not only consumes few memory in map updating but also can be easily implemented in parallel on GPUs. We have conducted the extensive evaluations on both public dataset and self-collected LiDAR sequences, whose promising results demonstrated that our proposed approach is very effective.

Currently, our method only takes considerations of LiDAR data, which may lead to the sensor degeneration in some cases. For future work, we will incorporating various sensors into an optimization framework.

## REFERENCES

- [1] J. Zhang and S. Singh, "Loam: Lidar odometry and mapping in real-time," in *Robotics: Science and Systems*, vol. 2, no. 9, 2014.
- [2] T. Shan and B. Englot, "Lego-loam: Lightweight and ground-optimized lidar odometry and mapping on variable terrain," in *2018 IEEE/RSJ International Conference on Intelligent Robots and Systems (IROS)*. IEEE, 2018, pp. 4758–4765.
- [3] J.-E. Deschaud, "Imls-slam: scan-to-model matching based on 3d data," in *2018 IEEE International Conference on Robotics and Automation (ICRA)*. IEEE, 2018, pp. 2480–2485.
- [4] J. Behley and C. Stachniss, "Efficient surfel-based slam using 3d laser range data in urban environments," in *Robotics: Science and Systems*, 2018.
- [5] X. Zheng and J. Zhu, "Efficient lidar odometry for autonomous driving," *IEEE Robotics and Automation Letters (RA-L)*, vol. 6, no. 4, pp. 8458–8465, 2021.
- [6] Z. Liu, F. Zhang, and X. Hong, "Low-cost retina-like robotic lidars based on incommensurable scanning," *IEEE/ASME Transactions on Mechatronics*, 2021.
- [7] D. Schubert, N. Demmel, L. von Stumberg, V. Usenko, and D. Cremers, "Rolling-shutter modelling for visual-inertial odometry," in *International Conference on Intelligent Robots and Systems (IROS)*, November 2019.
- [8] C. Park, P. Moghadam, S. Kim, A. Elfes, C. Fookes, and S. Sridharan, "Elastic lidar fusion: Dense map-centric continuous-time slam," in *2018 IEEE International Conference on Robotics and Automation (ICRA)*. IEEE, 2018, pp. 1206–1213.
- [9] J. Lin and F. Zhang, "Loam livox: A fast, robust, high-precision lidar odometry and mapping package for lidars of small fov," in *2020 IEEE International Conference on Robotics and Automation (ICRA)*. IEEE, 2020, pp. 3126–3131.
- [10] P. Dellenbach, J.-E. Deschaud, B. Jacquet, and F. Goulette, "Ct-icp: Real-time elastic lidar odometry with loop closure," *arXiv preprint arXiv:2109.12979*, 2021.
- [11] W. Gao and R. Tedrake, "Filterreg: Robust and efficient probabilistic point-set registration using gaussian filter and twist parameterization," in *Proceedings of the IEEE/CVF Conference on Computer Vision and Pattern Recognition*, 2019, pp. 11 095–11 104.
- [12] H. Wang, C. Wang, and L. Xie, "Lightweight 3-d localization and mapping for solid-state lidar," *IEEE Robotics and Automation Letters*, vol. 6, no. 2, pp. 1801–1807, 2021.
- [13] K. Li, M. Li, and U. D. Hanebeck, "Towards high-performance solid-state-lidar-inertial odometry and mapping," *IEEE Robotics and Automation Letters*, vol. 6, no. 3, pp. 5167–5174, 2021.
- [14] W. Xu and F. Zhang, "Fast-livox: A fast, robust lidar-inertial odometry package by tightly-coupled iterated kalman filter," *IEEE Robotics and Automation Letters*, vol. 6, no. 2, pp. 3317–3324, 2021.
- [15] D. Droschel and S. Behnke, "Efficient continuous-time slam for 3d lidar-based online mapping," in *2018 IEEE International Conference on Robotics and Automation (ICRA)*. IEEE, 2018, pp. 5000–5007.
- [16] P. J. Besl and N. D. McKay, "Method for registration of 3-d shapes," in *Sensor fusion IV: control paradigms and data structures*, vol. 1611. International Society for Optics and Photonics, 1992, pp. 586–606.
- [17] A. Censi, "An icp variant using a point-to-line metric," in *2008 IEEE International Conference on Robotics and Automation*. IEEE, 2008, pp. 19–25.
- [18] K.-L. Low, "Linear least-squares optimization for point-to-plane icp surface registration," *Chapel Hill, University of North Carolina*, vol. 4, no. 10, pp. 1–3, 2004.
- [19] A. Myronenko and X. Song, "Point set registration: Coherent point drift," *IEEE transactions on pattern analysis and machine intelligence*, vol. 32, no. 12, pp. 2262–2275, 2010.
- [20] A. Segal, D. Haehnel, and S. Thrun, "Generalized-icp," in *Robotics: science and systems*, vol. 2, no. 4. Seattle, WA, 2009, p. 435.
- [21] M. Magnusson, A. Lilienthal, and T. Duckett, "Scan registration for autonomous mining vehicles using 3d-ndt," *Journal of Field Robotics*, vol. 24, no. 10, pp. 803–827, 2007.
- [22] B. Jian and B. C. Vemuri, "Robust point set registration using gaussian mixture models," *IEEE transactions on pattern analysis and machine intelligence*, vol. 33, no. 8, pp. 1633–1645, 2010.
- [23] J. Sola, J. Deray, and D. Atchuthan, "A micro lie theory for state estimation in robotics," *arXiv preprint arXiv:1812.01537*, 2018.
- [24] W. Liu, H. Wu, and G. S. Chirikjian, "Lsg-cpd: Coherent point drift with local surface geometry for point cloud registration," in *Proceedings of the IEEE/CVF International Conference on Computer Vision*, 2021, pp. 15 293–15 302.
- [25] J. Lin and F. Zhang, "R3live: A robust, real-time, rgb-colored, lidar-inertial-visual tightly-coupled state estimation and mapping package," *arXiv preprint arXiv:2109.07982*, 2021.
- [26] Z. Liu and F. Zhang, "Balm: Bundle adjustment for lidar mapping," *IEEE Robotics and Automation Letters*, vol. 6, no. 2, pp. 3184–3191, 2021.